CFD simulations of multi-hole Diesel injector nozzle flow and sprays for various biodiesel blends

C. A. Chasos*, C. N. Christodoulou and G. N. Karagiorgis
Mechanical Engineering Department, Frederick University, Cyprus
eng.cca@fit.ac.cy, eng.cc@fit.ac.cy and eng.kg@fit.ac.cy

Abstract

The biodiesel physical properties, as well as the biodiesel blending percentage in Diesel fuel affect the injector nozzle flow and the emerging spray atomisation and spray characteristics. In the present study, the computational fluid dynamics (CFD) methodology is used to simulate the injector internal flow and the spray development for fuels at increasing biodiesel blending percentage in Diesel fuel. Four test fuels were examined, namely, pure diesel fuel, 10 % by volume of biodiesel blending in diesel fuel, 50 % by volume of biodiesel blending in diesel fuel and pure biodiesel, denoted B0, B10, B50 and B100, respectively. The Eulerian single-phase modelling methodology was used for the simulation of the fuel flow in a multi-hole Diesel injector. The Eulerian/Lagrangian two-phase flow modelling methodology was employed for simulations of the sprays produced by the four test fuels in a constant volume chamber, at atmospheric and high pressure and temperature conditions. From the injector internal flow simulations of the test fuels, the nozzle exit velocity was determined. The nozzle exit velocity and the physical properties of test fuels were used in an empirical expression to calculate the injected spray angles. The mass flow rate of the fuel, the nozzle geometry data and the spray angle were used as input in the Reitz-Diwakar spray atomisation model. The transient spray simulations were carried out using the Reitz-Diwakar spray atomisation model, along with the Reitz-Diwakar droplet break up model and O'Rourke inter-droplet collision model. From the simulations, it was found that cavitation takes place at the nozzle inlet for all test fuels and with increasing biodiesel blending percentage the turbulence level in the injector nozzle is reduced. The resulting spray angle decreases with increasing biodiesel blending percentage approximately by 20 % from pure diesel B0 to pure biodiesel B100 fuel. Comparisons of the simulated sprays of the test fuels were performed, and B0 and B100 sprays at high pressure and temperature chamber conditions were compared against published spray photographs and penetrations. It was found that the resulting spray penetration increases when the biodiesel blending percentage is increasing. From the validation against the experiments, the spray penetration was slightly overpredicted and the spray shape was wider than the experimental sprays, for both pure diesel and pure biodiesel sprays.

Introduction

There is recent interest for the utilisation of renewable and alternative fuels and this is regulated by the European Union (Directive 2009/30/EC), which for the case of biodiesel currently imposes a limit of 7% by volume biodiesel fuel blending in diesel fuel. The specifications of the biodiesel fuel used for blending diesel fuel should meet the European standard EN14214 [4]. The ranges and limits of density, viscosity and flash point of biodiesel are defined in EN14214. However, other properties important for fuel injection and spray atomisation, such as surface tension coefficient, vapour pressure, boiling point and latent heat of evaporation are not speficied in EN14214. Biodiesel physical properties, as well as the physical properties of different blends of biodiesel in diesel fuel are considered to affect the injector internal fuel flow, the spray atomisation and the atomised spray development.

The biodiesel physical properties, including density, dynamic viscosity, and surface tension coefficient have been investigated by [1], [7], [13] and [16]. At atmospheric conditions, the density of biodiesel compared to pure diesel fuel is around 5 to 10% higher, and the viscosity of biodiesel given at 40^{o}C is higher by almost factor of two than the viscosity of pure diesel. Limited data was presented for surface tension coefficient, which ranges from 0.025 to 0.03 N/m for biodiesel, while for diesel ranges approximately from 0.02 to 0.025 N/m. The effects of temperature on diesel and biodiesel fuel physical properties were investigated by Ra *et al* [13] over a range of temperatures between 300 to 1000 K.

Single-hole injectors as well as multi-hole Diesel injectors were used in experimental and computational studies. Injector internal flow and cavitation phenomena were investigated numerically in [6], [9], [12] and [15]. It was reported that for diesel fuel, the cavitation phenomena are more pronounced, because of the higher vapour pressure that diesel fuel exhibits compared to biodiesel fuel. However, further investigations are required for better understanding and validating the very complex phenomena of cavitation.

*Corresponding author: Dr. Charalambos Chasos: eng.cca@fit.ac.cy

The resulting sprays from diesel fuel and biodiesel blends were examined experimentally by [5], [8], [18] and [20] among others. It was found that the spray cone angle decreases and spray penetration increases with increasing blending percentage of biodiesel. Computational spray studies were performed by [11], [15] and [17] among others. It was reported that cavitating nozzle flow results in reduced spray penetration [17].

In the present study, the CFD methodology was employed, where the effects of biodiesel blending percentage in diesel fuel on the Diesel injector internal flow and spray characteristics were investigated. Four test fuels were examined, namely, pure diesel fuel, 10 % by volume of biodiesel blending in diesel fuel, 50 % by volume of biodiesel blending in diesel fuel and pure biodiesel, denoted B0, B10, B50 and B100, respectively.

Numerical methods and simulations setup

In the present section, firstly the modelling methodologies for the simulation of the injector internal flow and the spray simulation are briefly described. Then, the modelling approach adopted in the present study for linking the injector internal fuel flow with the spray atomisation by defining the injected spray angle is presented. The computational meshes employed for the simulations are illustrated, and the numerical details for the simulations of the injector internal flow and spray simulations are summarised.

The commercial CFD code STAR-CD [3] was employed for the investigations, and simulations were carried out using the Eulerian single-phase modelling methodology for the injector flow, while the Eulerian/Lagrangian two-phase flow modelling methodology was used for the spray simulations. For the injector internal flow, a steady-state simulation was performed during the phase of fully open needle of the injector. The transient spray simulations were carried out using the Reitz-Diwakar atomisation model [14], along with the Reitz-Diwakar droplet break up model [14] and O'Rourke inter-droplet collision model [10]. The collision model accounts for coalescence, separation and bouncing of spray droplets, and it was employed in the present study following Diesel spray simulation setup practices [2]. The k-ϵ RNG turbulence model [21] was used for both the internal injector flow and the spray simulations. For the simulations, the differencing scheme MARS was employed and the conjugate gradient algorithm [3] was used.

The mass flow rate of the fuel, the nozzle geometry data and the spray angle were used as input in the Reitz-Diwakar spray atomisation model. The cone angle for a Diesel jet non-evaporating liquid spray in the atomisation region is given by the following empirical formula (from Varde [19]):

$$tan\theta = A_1(\rho/\rho_l)^{1/3} Re_l^{1/3} We_l^{A_2} \ . \tag{1}$$

Here, A_1 and A_2 are coefficients given in Equations 4 and 5, ρ is the gas density, ρ_l is the liquid density, Re_l is the liquid Reynolds number and We_l is the liquid Weber number. The latter two quantities are defined respectively as:

$$Re_l = \frac{VD\rho_l}{\mu_l} \ , \tag{2}$$

$$We_l = \frac{V^2 D\rho_l}{\sigma} \ , \tag{3}$$

$$A_1 = \begin{cases} 0.0001(L/D)^5 \ , & \text{for } L/D < 6 \ , \\ \\ A_1 = 0.7 \ , & \text{for } L/D > 6 \ , \end{cases} \tag{4}$$

$$A_2 = \frac{3 - L/D}{3L/D} \ . \tag{5}$$

where V is the jet velocity assumed equal to the nozzle exit average velocity, D is the nozzle diameter, L is the nozzle orifice length, μ_l is the dynamic viscosity of the fuel and σ the surface tension coefficient of the fuel. The injector internal flow simulation provided the nozzle exit average velocity for the four test fuels examined.

For the investigations of the injector internal flow, a typical six-hole Diesel injector geometry was modelled and three-dimensional simulations of the injector internal flow were carried out for the test fuels. The holes were assumed to be symmetrically located around the periphery of the injector tip. The injector nozzle diameter and length were assumed 0.2 mm and 1 mm, respectively, resulting in a ratio of nozzle orifice length over nozzle diameter $L/D = 5$. For computational economy, only the symmetrical one sixth of the injector geometry was modelled using the block-structure approach for the three-dimensional mesh generation with hexahedral cells,

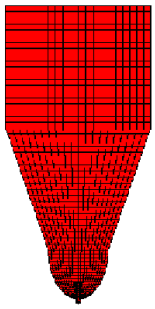

Figure 1. Injector mesh front view.

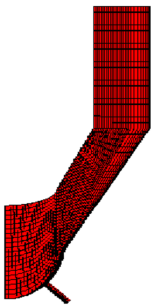

Figure 2. Injector mesh side view.

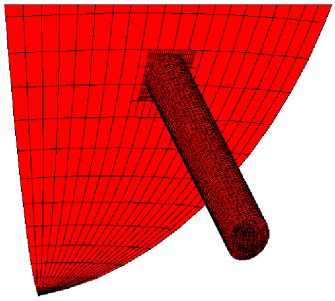

Figure 3. Injector mesh perspective view.

comprising a symmetrical mesh of 60° wedge angle. The mesh that was used for the simulations of the injector internal flow for the different test fuels is included in Figures 1, 2 and 3, which show the mesh front, side and perspective views, respectively. The total number of cells comprising the mesh was around 75000. The mesh was refined at the nozzle inlet area in order to capture the details of the flow at the region of nozzle inlet. The boundary conditions applied on the mesh, were inlet boundary at the top of the computational domain, symmetry plane boundary on both sides of the wedge mesh, pressure boundary at the nozzle exit and wall boundary on the remaining surfaces.

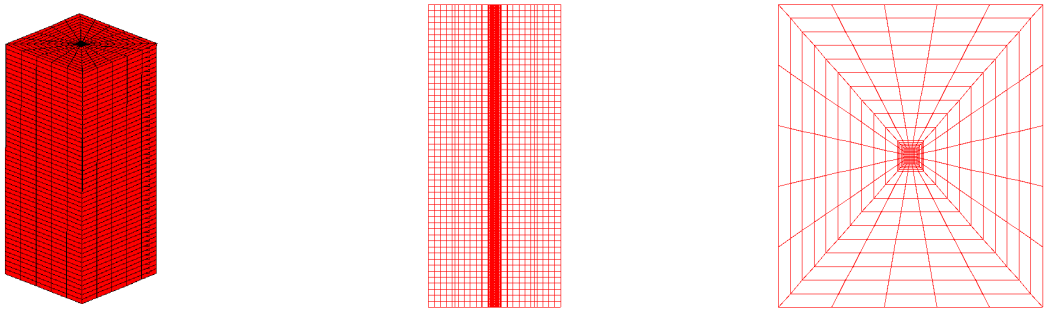

Figure 4. Constant volume chamber mesh perspective, side and top views.

The computational mesh for the constant volume chamber spray simulations is shown in Figure 4, where its height is 200 mm, width is 100 mm and length is 100 mm. The mesh was composed of 70000 hexahedral cells. The mesh was refined at the central region, where the the spray was injected and evolved, where the minimum cell side was 0.5 mm. The spray that emerged from one of the six nozzles of the injector was only modelled and simulated. The nozzle exit was located at the centre of the top surface of the mesh. The boundary conditions employed were slip wall boundary at the top surface of the mesh of the chamber, pressure boundary at the bottom of the mesh of the chamber and no-slip wall boundaries at the four side surfaces of the chamber. The droplet parcels introduction rate was 5 $parcels/\mu s$ and the time step size was 2 μs.

The same amount of fuel of 20 mm^3 was assumed to be injected for an injection duration of 3 ms. At atmospheric conditions, the fuel density of B0, B10, B50 and B100 was 860, 864, 880 and 900 Kg/m^3, respectively. The molecular viscosity was assumed 0.00215, 0.002376, 0.00324 and 0.0045 Kg/ms, for B0, B10, B50 and B100, respectively. The surface tension coefficient was set to 0.025, 0.0255, 0.0275 and 0.03 N/m for B0, B10, B50 and B100, respectively. It was assumed that test fuel and vapour properties have the same dependence on temperature with n-octane and data for biodiesel properties were selected from literature [13], [4]. The fuel properties of the test fuels differ, and it is expected to result in different nozzle flow, primary atomisation and spray droplet behaviour.

Results and discussion

First, the results from the injector internal flow simulations are presented followed by the spray simulations in the constant volume chamber for atmospheric conditions for the test fuels. Then, the comparisons of simulated sprays with B0 and B100 against experimental data at high pressure and temperature conditions of the constant volume chamber are illustrated.

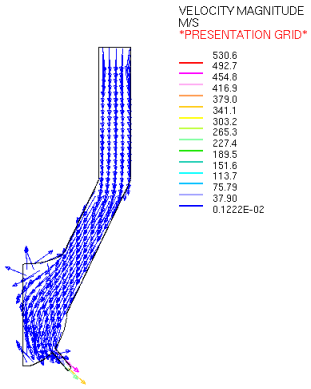

Figure 5. B0 velocity field at the symmetry section plane of the nozzle.

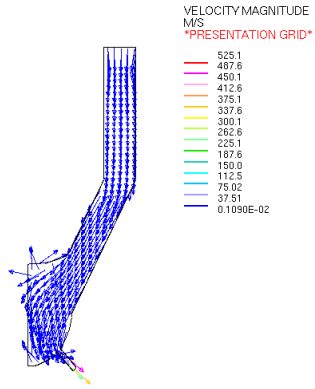

Figure 6. B100 velocity field at the symmetry section plane of the nozzle.

Figures 5 and 6 show the velocity prediction at the symmetry section plane of the mesh for the test fuels B0 and B100, respectively. It can be observed that the flow structure is similar, and that the maximum fuel velocity slightly decreased by approximately 1% when the biodiesel blending percentage increased from zero in diesel B0 to 100% in biodiesel B100. The trend is that fuel velocity slightly decreases with increasing biodiesel blending percentage. Also, the recirculation zone observed at the tip of the injector slightly decreases for increasing biodiesel blending percentage. Views of the velocity fields for B0 and B100 test fuels are presented in Figures 7 and 8, where the

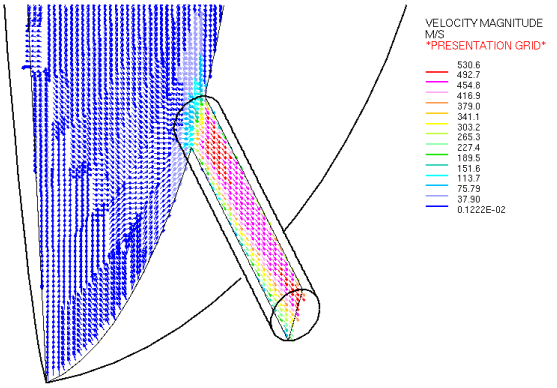

Figure 7. B0 velocity field at the symmetry section plane of the nozzle.

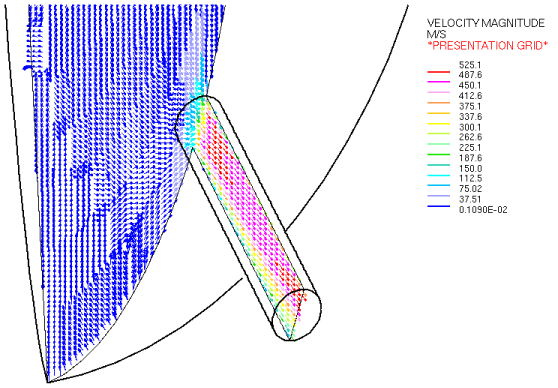

Figure 8. B100 velocity field at the symmetry section plane of the nozzle.

nozzle area is zoomed at the symmetry section plane plotted at perspective view. It can be seen that the velocity fields are similar, and the higher velocities of the field are displaced towards the upper edge of the nozzle, due to the effect of the upstream flow and the flow into inlet of the nozzle. Views of the velocity fields for B0 and B100 test fuels at the section plane normal to the symmetry section plane are shown in Figures 9 and 10. It can be seen that the velocity profiles are similar and almost symmetrical for the test fuels.

The ratio of the predicted turbulent viscosity over the molecular viscosity μ_t/μ is shown in Figures 11 and 12 for B0 and B100 test fuels, respectively. The levels of turbulence are higher for pure diesel fuel than the levels of turbulence for pure biodiesel. In Figures 11 and 12, it can be seen that the ratio μ_t/μ decreased by more than 5% when the biodiesel blending percentage increased from zero in pure diesel to 100% in pure biodiesel B100. The higher levels of turbulence in the nozzle for pure diesel than pure biodiesel are expected to affect more the downstream fuel jet atomisation.

The calculated pressure fields for B0 and B100 at the symmetry section plane of the injector mesh are shown in Figures 13 and 14, respectively. From the predicted pressure fields, it can be observed that zones with pressures lower than atmospheric pressure occur at the upper and lower edge of the nozzle inlet for the test fuels. This observation reveals that cavitation takes place at the nozzle inlet area, which is expected to affect the jet emerging from nozzle and spray atomisation. However, cavitation phenomena should be examined using cavitation modelling, in order to quantify the effects of biodiesel blending percentage on cavitation.

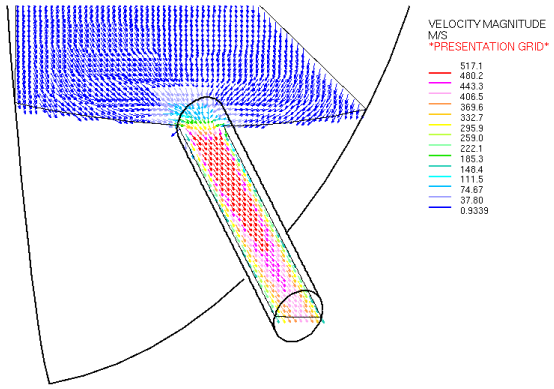

Figure 9. B0 velocity prediction at the normal section plane of the nozzle.

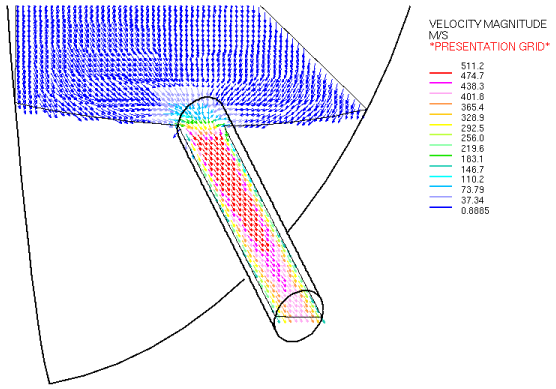

Figure 10. B0 velocity prediction at the normal section plane of the nozzle.

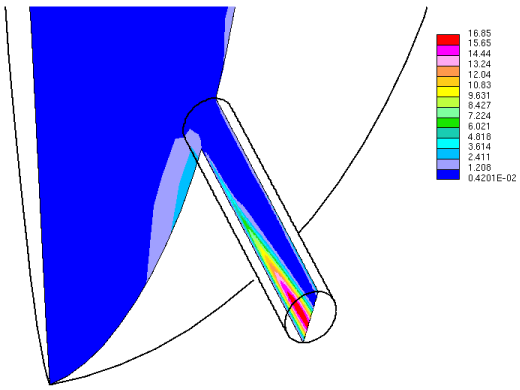

Figure 11. B0 ratio of turbulent viscosity over molecular viscosity μ_t/μ at the symmetry section plane of the nozzle.

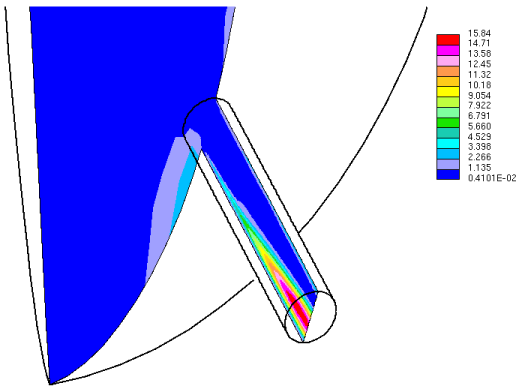

Figure 12. B100 ratio of turbulent viscosity over molecular viscosity μ_t/μ at the symmetry section plane of the nozzle.

From the injector internal flow simulations, the velocity predictions were used to calculate the average velocity normal to the nozzle exit cross-sectional area. The average velocity, the fuel properties and the constant volume chamber density were used in Equation 1 to calculate the spray cone angle θ, in order to link the nozzle flow with the emerging spray atomisation and structure. The nozzle exit average velocity is given in Table 1, which slightly decreases with increasing biodiesel blending percentage. The calculated spray cone angle of atmospheric and high pressure and temperature chamber conditions is also included in Table 1. The spray cone angle which depends on the average velocity at nozzle exit, the chamber conditions and the fuel properties of the test fuels decreases with increasing biodiesel blending percentage. For atmospheric chamber conditions, the spray cone angle θ_{atm} is approximately by a factor of two smaller than the spray cone angle θ_{high} at high pressure and temperature chamber conditions. Furthermore, for both atmospheric and high pressure and temperature conditions, the spray cone angle decreased approximately by 20%, when the fuel was pure diesel and became pure biodiesel.

The comparisons of simulated sprays with the four test fuels in atmospheric chamber conditions at 1.5 ms after the start of injection (ASOI) are shown in Figure 15. The predicted parcels of spray droplets are plotted in colour and are scaled according to their diameter. From Figure 15, it can be seen that near the nozzle exit the spray is narrow and further downstream at the region of the spray body the spray widens because of the droplet breakup and collision phenomena and the interaction with the induced gas flow field. At the tip of the spray, the structure of the droplets is narrow. Similar spray patterns are observed for all the test fuels with two trends, first the body of the spray slightly narrows and second the spray tip penetration slightly increases with increasing biodiesel blending percentage.

Spray photographs and spray penetration data were selected from published experiments [8]. The spray experiments were carried out with B0 and B100 fuels in high pressure and temperature chamber conditions, and data at 1.5 ms ASOI was available. The cases of B0 and B100 test fuels were modelled for chamber conditions same to the experiments, with chamber pressure of 42 bar and temperature of 1000 K. The simulations of B0 and B100 sprays

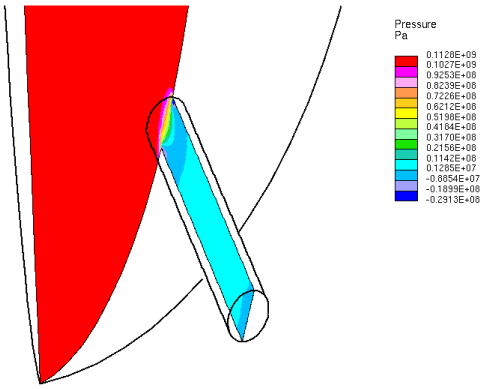

Figure 13. B0 pressure field at the symmetry section plane of the nozzle.

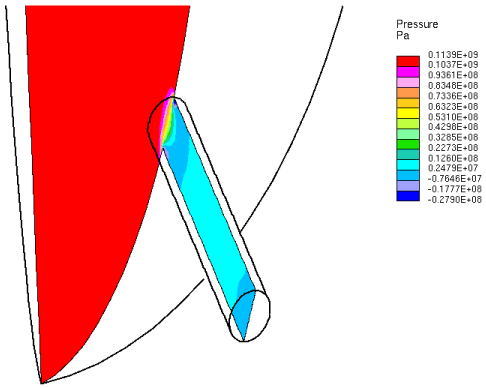

Figure 14. B100 pressure field at the symmetry section plane of the nozzle.

$Fuel$	$V(m/s)$	θ_{atm}	θ_{high}
B0	241.2	9.4	21.2
B10	240.6	9.1	20.6
B50	238.5	8.3	18.9
B100	235.8	7.5	17.2

Table 1. Nozzle exit average velocity and spray cone angle at atmospheric conditions θ_{atm} and at high pressure and temperature conditions θ_{high}.

were carried out using the mesh employed for the atmospheric sprays, and the boundary and initial conditions corresponding to the high pressure and temperature conditions of the experiment were applied. Figure 16 includes the comparisons of the predicted sprays against the spray photographs at 1.5 ms ASOI. The spray photographs in Figure 16 have a view field height of 50 mm and are scaled 1:1 to the mesh height. The photographs show the illuminated spray droplets at the body of the spray, and droplets that are located around the body and at the tip of the spray may not be captured by the experiment. The plots of simulated spray show all the injected droplet parcels with a visible size that is bigger than their real size, which results in wider spray shape and higher tip penetration than the experiment. Furthermore, in Figure 16, it can be observed that the simulated spray produced with biodiesel penetrates further downstream and it is narrower than the simulated spray with pure diesel. The prediction of increased spray penetration with increasing biodiesel blending percentage agrees with the experiment. However, the predicted spray shapes are found wider than the experimental spray shapes. Thus, comparisons of the calculated spray cone angle against experiments and additional validation studies for spray shape and penetration are required.

Figure 17 contains the comparisons of spray penetration between the simulations with B0 and B100 and the experimental data. The penetrations from the experiment were measured from the spray photographs at 1.5 ms ASOI. The penetration definition for the simulation was set as the vertical line to the nozzle symmetry line, behind which the 90% of the total mass of injected spray droplets resides. For both test fuels, spray penetration is slightly overpredicted and is in good agreement with the trend observed in the experiment, where biodiesel penetration is higher than diesel penetration. In Figure 17, it can be seen that until 0.5 ms ASOI, the predicted penetration for biodiesel is slightly higher than the predicted penetration for diesel, and from 0.7 ms ASOI the difference in spray penetration between diesel and biodiesel increases. From 1 ms ASOI, the rate of increase of spray penetration is reduced. The differences between diesel and biodiesel sprays are due to the different droplet physical properties and the evaporation behaviour which result in different droplet size and velocity and different induced gas flow fields.

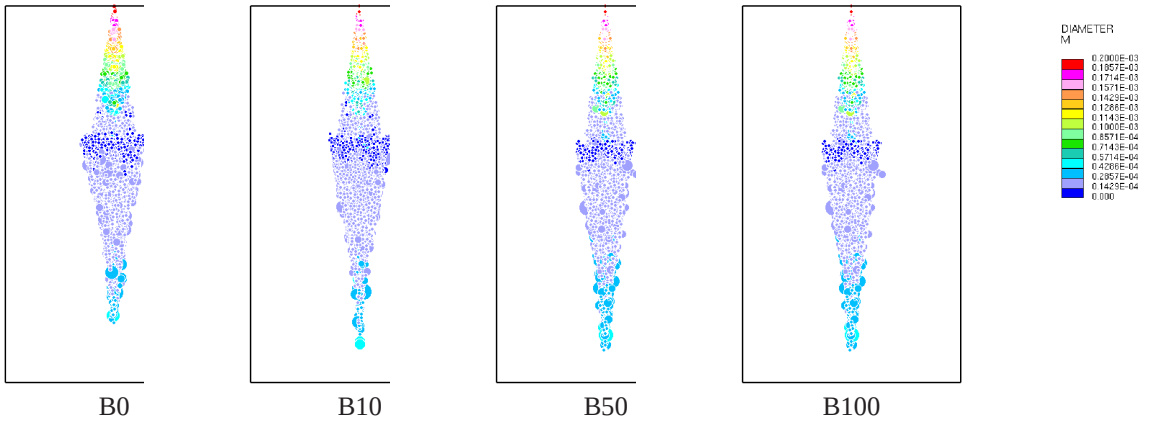

Figure 15. B0, B10, B50 and B100 simulated sprays in atmospheric chamber at 1.5 ms ASOI.

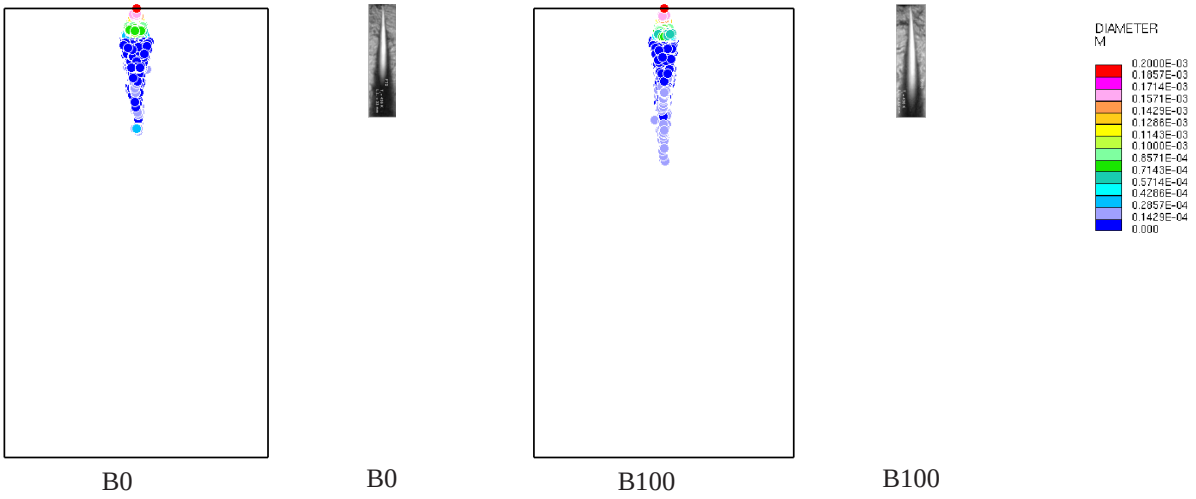

Figure 16. B0 and B100 predicted spray comparisons with photographs in high pressure and temperature chamber at 1.5 ms ASOI.

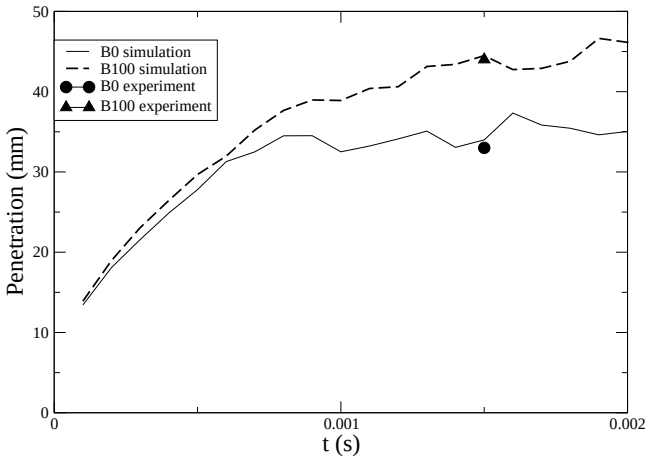

Figure 17. B0 and B100 spray penetration validation at high pressure and temperature chamber.

Summary and conclusions

In the present study, the CFD methodology was used to simulate the injector internal flow and the spray development for four test fuels at increasing biodiesel blending percentage in Diesel fuel. The Eulerian single-phase modelling methodology was used for the simulation of the fuel flow in a mutli-hole Diesel injector and the Eulerian/Lagrangian two-phase flow modelling methodology was employed for simulation of the sprays.

From the injector simulations, it was found that the nozzle exit velocity slightly decreases and the turbulence level in the nozzle is reduced with increasing biodiesel blending percentage, while cavitation takes place at the nozzle inlet. The resulting spray angle decreases with increasing biodiesel blending percentage. From the spray simulations, it was found that the resulting spray penetration increases when the biodiesel blending percentage is increasing. Validations of simulated sprays at high pressure and temperature conditions against experimental spray photographs and penetrations showed that penetration is slightly overpredicted and the spray body shape is wider than the experimental spray.

For future work, detailed internal geometry of Diesel injectors, the injector needle lift history, experimental measurements of the fuel mass flow rate history and detailed data of fuel and vapour properties should be used. Validation studies should be performed, including comparisons with detailed experimental data of spray angle, spray shape and penetration, droplet size and velocity and fuel vapour pattern. Modelling and simulation of cavitation in the nozzle should be performed, and other existing state-of-the-art spray atomisation models should be examined. Furthermore, other modelling methodologies should be used including the volume of fluid method for transient internal two-phase flow simulation of Diesel injector.

Acknowledgements

The provision of computer facilities by Frederick University is acknowledged.

References

[1] Anitescu, G., Bruno, T. J., *The Journal of Supercritical Fluids.* 63:133-149 (2012).
[2] Clerides, D. *Numerical simulation of spray processes in diesel engines.* PhD Thesis, University of London. (1997).
[3] Computational Dynamics adapco Ltd., *STAR-CD Methodology, Version 4.14.* London, England. (2011).
[4] Cyprus Organisation for Standardisation (CYS), *CYS EN 14214:2008+A1: Automotive fuels - Fatty acid methyl esters (FAME) for diesel engines - Requirements and test methods.* (2009).
[5] Fang, T., Lin, Y. C., Foong, T. M., Lee, C. F., *Fuel.* 88:2154-2162 (2009).
[6] Gogoi, T. K., Baruah, D. C., *Energy.* 35:1317-1323 (2010).
[7] Hoekman, S. K., Broch, A., Robbins, C., Ceniceros, E., Natarajan, M., *Renewable and Sustainable Energy Reviews.* 16:143-169 (2012).
[8] Higgins, B. S, Mueller, C. J., Siebers, D. L., *SAE Technical Paper Series 1999-01-0519.* (1999).
[9] Margot, X., Hoyas, S., Fajardo, P.,Patouna, S., *Mathematical and Computer Modelling.* 52:1143-1150 (2010).
[10] O' Rourke, P. J. *Collective Drop Effects on Vaporising Liquid Sprays.* PhD Thesis, University of Princeton. (1981).
[11] Park, S. H., Kim, H. J., Suh, H. K.,Lee, C. S., *International Journal of Heat and Fluid Flow.* 30:960-970 (2009).
[12] Payri, F., Payri, R., Salvador, F. J., Lopez, J. M., *Computers & Fluids.* 58:88-101 (2012).
[13] Ra, Y., Reitz, R. D., Mc Farlane, J., Daw, C., S., *SAE Technical Paper Series 2008-01-1379.* 1:1 (2008).
[14] Reitz, R. D., Diwakar, R., *SAE Technical Paper Series 860469.* (1986).
[15] Som, S., Longman, D. E., Ramirez, A. I., Aggaral, S. K., *Fuel.* 89:4014-4024 (2010).
[16] Tesfa, B., Gu, F., Powles, N., *Renewable Energy.* 35:2752-2760 (2010).
[17] Tonini, S., Gavaises, M., Theodorakakos, A., *International Journal of Thermal Sciences.* 48:554-572 (2009).
[18] Valentino, G., Alloca, L., Iannuzzi, S.,Montanaro, A., *Energy.* 36:3924-3932 (2011).
[19] Varde, K. S., *The Canadian Journal of Chemical engineering.* 63 (1985).
[20] Wang, X., Huang, Z., Kuti, O. A., Zhang, W., Nishiba, K., *International Journal of Heat and Fluid Flow.* 31:659-666 (2010).
[21] Yakhot, V., Orszag, S. A., *Journal of Scientific Computing.* 1:1-51 (1986).